remote sensing

MDPI

Article

Improved Bi-Angle Aerosol Optical Depth Retrieval Algorithm from AHI Data Based on Particle Swarm Optimization

Chunlin Jin [1], Yong Xue [1,2,3,*], Xingxing Jiang [1], Yuxin Sun [1] and Shuhui Wu [1]

1 School of Environment and Spatial Informatics, China University of Mining and Technology, Xuzhou 221116, China; ChunlinJ@cumt.edu.cn (C.J.); XXJ@cumt.edu.cn (X.J.); sunyx@cumt.edu.cn (Y.S.); Wush@cumt.edu.cn (S.W.)
2 School of Computing and Engineering, University of Derby, Derby DE22 1GB, UK
3 Artificial Intelligence Research Institute, China University of Mining and Technology, Xuzhou 221116, China
* Correspondence: y.xue@derby.ac.uk; Tel.: +86-139-1053-5998

Abstract: The Advanced Himawari Imager (AHI) aboard the Himawari-8, a new generation of geostationary meteorological satellite, has high-frequency observation, which allows it to effectively capture atmospheric variations. In this paper, we have proposed an Improved Bi-angle Aerosol optical depth (AOD) retrieval Algorithm (IBAA) from AHI data. The algorithm ignores the aerosol effect at 2.3 µm and assumes that the aerosol optical depth does not change within one hour. According to the property that the reflectivity ratio K of two observations at 2.3 µm does not change with wavelength, we constructed the equation for two observations of AHI 0.47 µm band. Then Particle Swarm Optimization (PSO) was used to solve the nonlinear equation. The algorithm was applied to the AHI observations over the Chinese mainland (80°–135°E, 15°–60°N) between April and June 2019 and hourly AOD at 0.47 µm was retrieved. We validated IBAA AOD against the Aerosol Robotic Network (AERONET) sites observation, including surrounding regions as well as the Chinese mainland, and compared it with the AHI L3 V030 hourly AOD product. Validation with AERONET of 2079 matching points shows a correlation coefficient R = 0.82, root-mean-square error RMSE = 0.27, and more than 62% AOD retrieval results within the expected error of $\pm(0.05 + 0.2 \times AOD_{AERONET})$. Although IBAA does not perform very well in the case of coarse-particle aerosols, the comparison and validation demonstrate it can estimate AHI AOD with good accuracy and wide coverage over land on the whole.

Keywords: AHI AOD; IBAA; PSO

Citation: Jin, C.; Xue, Y.; Jiang, X.; Sun, Y.; Wu, S. Improved Bi-Angle Aerosol Optical Depth Retrieval Algorithm from AHI Data Based on Particle Swarm Optimization. *Remote Sens.* **2021**, *13*, 4689. https://doi.org/10.3390/rs13224689

Academic Editor: Carmine Serio

Received: 3 November 2021
Accepted: 18 November 2021
Published: 20 November 2021

1. Introduction

Aerosols are solid and liquid particles suspended in the atmosphere with a particle size between 0.001 and 100 µm. They come from a wide range of sources, including natural and anthropogenic source aerosols, such as pollen, sea salt particles, dust, smoke, haze, and so on. The scattering and absorption effects of aerosols directly affect radiation reaching the earth and atmospheric temperature, which is of great significance to the study of global climate change and radiative forcing [1,2]. Furthermore, heavy aerosol loading reduces atmospheric visibility and causes harm to people's health [3]. Therefore, it is necessary to monitor the state of atmospheric aerosols. Although there are many ground-based monitoring stations, such as AERONET (Aerosol Robotic Network) and SONET (Sun-sky radiometer Observation Network) observation networks, which can obtain accurate aerosol information, they are too sparse to meet the needs of large-scale monitoring over a long period of time. Retrieving aerosol information from satellite observation is an effective solution to solve the problem. Geostationary meteorological satellites can provide high-frequency observations with broad coverage. Thus, they can monitor the evolution of sandstorms and the occurrence, dissipation, and movement of haze in near real-time [4–6].

Aerosol optical depth (AOD) is one of the most important aerosol properties and is widely recognized as a critical indicator in understanding atmospheric physics and regional air quality [7]. There have been many studies on the quantitative measurement of AOD using geostationary satellite observations. Knapp et al. (2005) obtained AOD of GOES-8 (Geosynchronous Earth Orbit Satellite) in the United States every 30 min using the time-series method [8]. The time-series method determined the surface contribution from temporal compositing of visible imagery with a 14-day window, where darker pixels correspond to less atmospheric attenuation and surface reflectance is deduced from the composite using radiative transfer. In addition, the method has also been applied to the Spinning Enhanced Visible and InfraRed Imager (SEVIRI) aboard the Meteosat Second-Generation (MSG) satellite [9], Geostationary Ocean Color Imager (GOCI) onboard the Communication, Ocean, and Meteorological Satellite (COMS) [10,11], MTSAT-1R [12], CMOS/ Meteorological Imager (MI) [13], etc. Though the time-series method has been used widely, the selection of reflectance over the time window is uncertain due to the existence of clouds and shadows and the complex relationship between aerosol, surface reflectance, and the top of atmosphere reflectance (TOAR) [8].

Moreover, the surface reflectance changes during a period cannot be ignored. Relying on the high-frequency observation characteristics of the geostationary satellite, certain multi-temporal and multi-angle algorithms have been successfully applied to geostationary satellite AOD inversion. Thomas et al. (2009) applied the AATSR (Advanced Along-Track Scanning Radiometer) ORAC (Oxford-RAL retrieval of Aerosols and Clouds) algorithm to SEVIRI AOD inversion [14]. Zhang et al. (2011) applied the MAIAC algorithm to GOES observation and obtained the surface bidirectional reflectance distribution function and AOD [15]. Mei et al. (2012) utilized the k-ratio approach (k-ratio is the ratio of surface reflectance for two subsequent observations, which was approximated by the ratio of the reflectance at 1.6 μm) and time-series technique for joint retrieval of AOD and aerosol type from MSG/SEVIRI [16]. Additionally, the optimal estimation (OE) method is used to invert AOD and the surface bidirectional reflectance factor [17]. Zhang et al. (2020) used an empirical bias correction algorithm to improve the diurnal bias in the GOES-16 Advanced Baseline Imager AOD due to deficiencies in the land-surface–reflectance relationship currently applied in the ABI AOD retrieval algorithm [18], which is developed from the Dark Target (DT) algorithm [19]. It is worth noting that Xie et al. (2019) derived a global and hourly dataset of AOD from GOES-16, MSG-1, MSG-4, and Himawari-8 [20]. For Himawari-8 AHI AOD, the famous DT algorithm was tested and produced a good result [21–23]. She et al. (2018) obtained the hourly AOD and surface reflectance by the OE method [24]. Su et al. (2020) proposed an algorithm combining DT and DB (Deep Blue) by building a monthly spectral base reflectance ratio library, which is a ratio library of 0.47 μm and 0.51 μm to 2.3 μm [25]. Many other studies have also greatly enriched AHI aerosol inversion [26–29].

This paper is based on the theory of a bi-angle approach to retrieve the earth's surface albedo proposed by Xue and Cracknell (1995) [30], which has been applied to MODIS (Moderate Resolution Imaging Spectroradiometer) AOD retrieval [31,32]. In this paper, we make the following assumptions: (1) AOD does not vary over one hour; (2) AHI observations at 2.3 μm are not affected by aerosols; and (3) the surface reflectance ratio of the two observations does not depend on wavelength. Then, based on the simultaneous equations of two observations, we used particle swarm optimization to solve the optimal solution. The framework of the paper is as follows: Section 2 presents the introduction of the data used in the paper. Section 3 shows the detailed algorithm including the basic theory of the bi-angle approach, PSO, and the process of AHI AOD retrieval. Section 4 describes the algorithm results and validation results and the change of surface albedo. The section also analyzes the setting of PSO boundaries and IBAA performance in a coarse aerosol situation. The conclusion is given in Section 5 and the future plan is also discussed in this part.

2. Data

In this paper, we used Himawari-8 L1 2 KM gridded data and L3 V030 hourly AOD, MODIS L2 10 KM AOD, MCD12C1 land cover type data, and ground-based aerosol monitoring network AERONET data. The detailed data description is as follows.

2.1. Himawari-8 AHI Data

Himawari-8 is a new-generation geostationary meteorological satellite launched by the Japan Meteorological Agency (JMA) in October 2014. AHI onboard the satellite can observe at 120° × 120° (80°E–20°W, 60°N–60°S), covering East Asia, the Western Pacific Ocean, Australia, and other large areas. It provides observations every 10 min with 16 bands and high spatial resolution. In the study, Himawari-8 L1 data, which have been corrected for radiation and gridded at 2 km, were used for algorithm testing, and Japan Aerospace Exploration Agency (JAXA) L3 V030 products were used for comparison [33,34]. These data can be downloaded free from the JAXA Himawari Monitor (https://www.eorc.jaxa.jp/ptree/index.html, last accessed date: 19 November 2021).

2.2. MODIS Data

MODIS sensors aboard Terra and Aqua have been widely used in many research fields. They can provide visible observations twice every day. In this paper, we used MODIS Collection 6.1 10 km aerosol products, which provide AOD from DT and DB algorithms, and combined AOD from DB and DT [35]. These MODIS AOD products have good accuracy in China [36–38]. The combined AOD was used to calculate the maximum value of each month in the region and DB AOD was used to compare with IBAA AOD at 0.47 µm. The MCD12C1 product provides the dominant land cover type and sub-grid frequency distribution of land cover classes. It is mainly applied to the water mask. These products can be obtained from the website https://ladsweb.modaps.eosdis.nasa.gov (last access: 19 November 2021)).

2.3. AERONET Data

AERONET is a global ground-based remote sensing aerosol observation network established by NASA and PHOTONS. It provides a long-term, continuous, and readily accessible public domain database of aerosol optical, microphysical, and radiative properties for aerosol research and characterization. The available Version 3 AERONET AOD data are computed for three data quality levels: Level 1.0 (unscreened), Level 1.5 (cloud-screened), and Level 2.0 (cloud screened and quality-assured) [39]. In order to evaluate the IBAA algorithm more comprehensively in space, as Figure 1 shows, we have selected 14 AERONET stations (Level 2.0 products are preferred; if not, level 1.5 products are chosen) in the Chinese mainland and surrounding areas for IBAA AOD validation. The distribution of selected stations is shown in Figure 1.

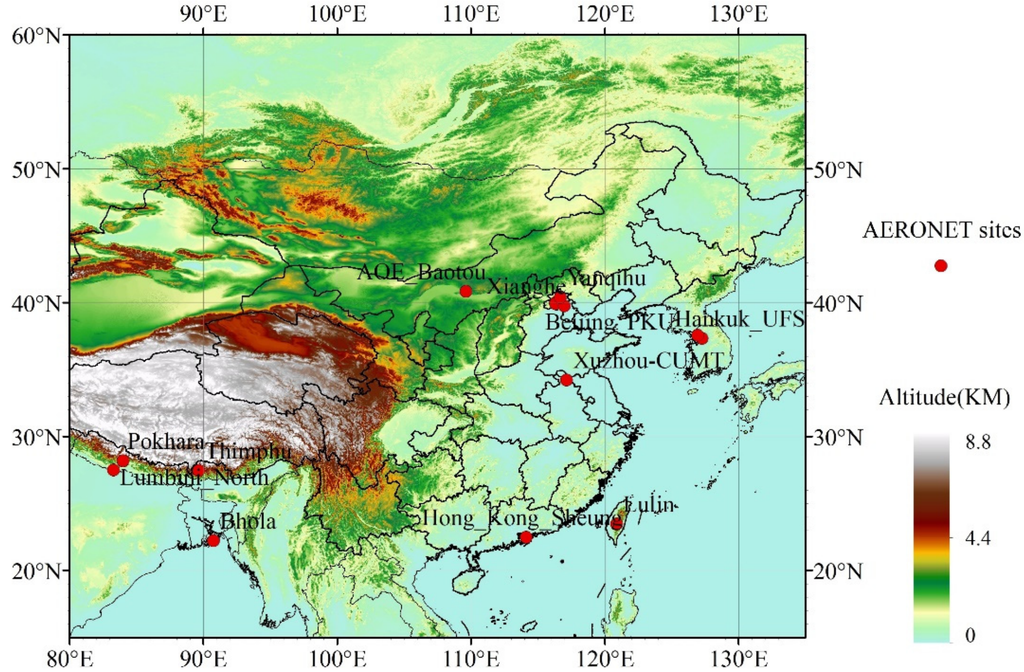

Figure 1. Study area. The solid red circles represent the locations of AERONET sites, and the color strip shows the altitude of the study area.

3. Principle and Method

3.1. Theory of Bi-Angle AOD Inversion

In 1995, Xue and Cracknell (1995) proposed an operational bi-angle approach to retrieve the earth surface albedo from AVHRR data [30]. They obtained a formula for the relationship between the surface albedo and the atmospheric optical depth by solving the radiative transfer equation. The formula is as follows.

$$A = \frac{(A'b - a) + a(1 - A')e^{[(a-b)\varepsilon\tau_0^\lambda \sec\theta']}}{(A'b - a) + b(1 - A')e^{[(a-b)\varepsilon\tau_0^\lambda \sec\theta']}} \tag{1}$$

where A is the surface albedo and A' is the apparent reflectance at wavelength λ. $a = \sec\theta$, $b = 2$, ε is the backscattering coefficient, designed to be 0.1 according to previous studies [30–32]. τ_0^λ is the atmospheric optical depth and $\tau_0^\lambda = \tau_r + \tau_a$, where τ_r is the Rayleigh optical depth that can be accurately calculated by $\tau_r = 0.00864 \cdot \lambda^{(-3.916+0.074\lambda+0.05/\lambda)}$ (the units for λ is micrometer) and τ_a is the atmospheric aerosol optical depth. θ represents the solar zenith angle and θ' denotes the zenith angle of the sensor.

For a single observation of a single band, there are two unknown parameters, AOD and surface albedo. In this study, AOD and surface albedo were retrieved using an aerosol-sensitive 0.47 μm band. The 0.47 μm band is more sensitive to aerosols because it samples a part of the electromagnetic spectrum where clear-sky atmospheric scattering is important. It is assumed that AOD does not change in the observation interval of one hour, which is consistent with the verification of ground stations [40]. Then, we ignored the aerosols influence in 2.3 μm band, that is, the apparent reflectance is assumed to be equal to its surface albedo. The error analysis of coarse-particle aerosols is given in Section 4. Some studies have shown that the surface reflectance ratio of two observations is only related to the geometric influence factor, which is independent of wavelength [41,42]. It can be expressed as Equation (2). K is the ratio of two observations at 2.3 and 0.47 µm. $A^1_{0.47\mu m}$ and $A^2_{0.47\mu m}$ represent the first and second observations at 0.47 µm.

$$K = \frac{A^1_{2.3\mu m}}{A^2_{2.3\mu m}} = \frac{A^1_{0.47\mu m}}{A^2_{0.47\mu m}} \tag{2}$$

Thus, the hourly AOD and the surface albedo can be calculated according to two observations with an interval of one hour. It is necessary to note that, since two observations are involved, accurate pixel location matching is very important. AHI's positioning accuracy is less than 1 km with stability and effectiveness [43]. However, this positioning accuracy is too rough for the 2 km resolution in the joint inversion with two observations. In order to reduce the error caused by pixel matching, we reduce the AHI spatial resolution to 10 km.

3.2. Particle Swarm Optimization

Among the existing inverse numerical solutions based on physical models, direct iterative solutions and optimization methods are widely applied [24,44,45]. These algorithms involve iterative processes that require an initial value, and in some cases where the truth value is far from the initial value, larger deviations tend to occur [46–48]. Particle Swarm Optimization (PSO) is a bionic algorithm proposed by Kennedy and Eberhart in 1995 [49]. It is a random search algorithm based on group cooperation and it does not need to be given an initial value, but a valid range to effectively solve the optimal solution.

PSO simulates a flock of birds searching for food at random. With only one piece of food in the area, none of the birds know where the food is. However, they know how close they are to the food, and the easiest and most effective way is to search the area around the bird closest to the food. In the PSO algorithm, the solution of each optimization problem is a bird in the search space, called a "particle". It is initialized as a group of random particles (random solutions), and then the optimal solution is found through iteration: The bird is abstracted as a particle (point) without mass and volume, and extended to the N-dimensional space. The position of particle i in the N-dimensional space is expressed as the vector $X_i = (X_{i1}, X_{i2} \cdots X_{iN})$, and the flight speed is expressed as the vector $V_i = (V_{i1}, V_{i2} \cdots V_{iN})$. Each particle has a fitness value determined by the objective function and knows the best position and the current position (X^k_{id}) it has found so far. This can be thought of as the particle's own flight experience. In addition, each particle knows the best position found so far for all the particles in the entire population. This can be thought of as the experience of particle companions. The particle is determined by its own experience and the best experience of its peers. The PSO algorithm can be boiled down to the following two iteration processes.

$$V^{k+1}_{id} = \omega V^k_{id} + c_1 r_1 \left(P^k_{id} - X^k_{id}\right) + c_2 r_2 \left(P^k_{gd} - X^k_{id}\right) \tag{3}$$

$$X^{k+1}_{id} = X^k_{id} + V^{k+1}_{id} \tag{4}$$

where i is the ith particle in the solution space, d is the dth dimension of the N-dimension, and k refers to the kth iteration. V is the velocity of the particle and ω is the inertia weight factor, which is a constant greater than zero, determining the global and local optimization capabilities. c_1 and c_2 are the acceleration constants. r_1 and r_2 are random numbers distributed in the interval [0,1]. P^k_{id} represents the dth dimension of the best position (value) of the ith particle in the kth iteration and P^k_{gd} denotes the dth dimension of the global optimal solution at the kth iteration.

For the optimization solution of the mentioned variables, PSO randomly initializes multiple group solutions (random particles). By constructing the cost function, every group solution's fitness is calculated. The overall flow of the PSO algorithm is shown in the Figure 2. It is simple, easy to implement, has fewer parameters, no gradient information, performs well in a variety of complex optimization problems, and it has been widely used in many fields [50–53]. In this study, we applied it to jointly retrieve AOD and the surface albedo from AHI.

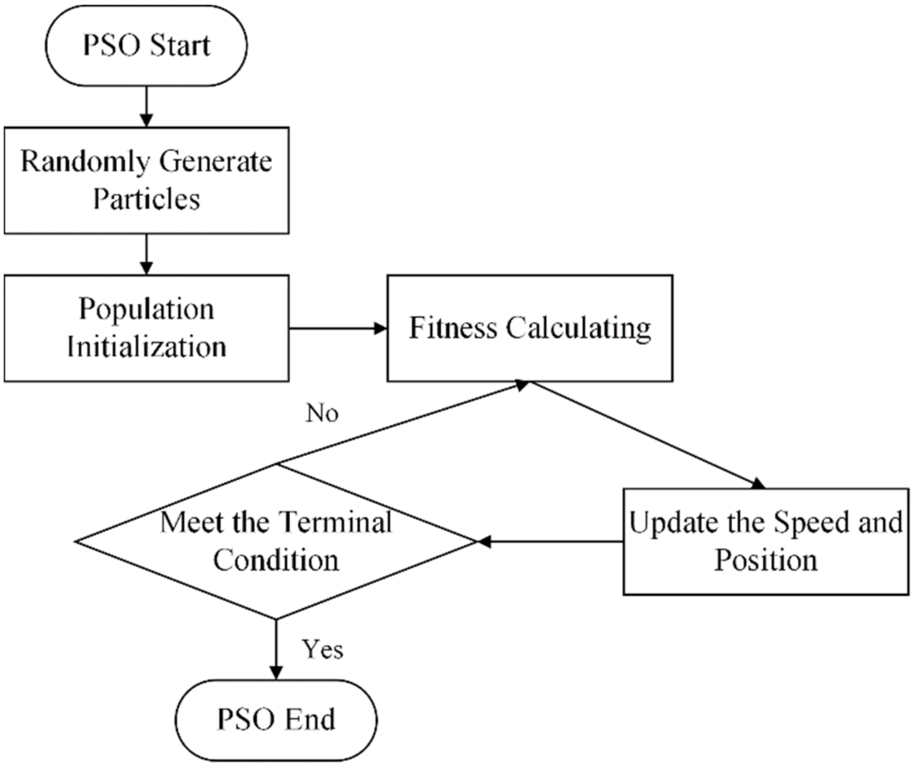

Figure 2. The flow chart of PSO.

3.3. *IBAA Algorithm Scheme*

The study focuses on AOD retrieval of AHI over the Chinese mainland, and the geographical range is 80°E–135°E, 15°N–60°N. Figure 1 shows the elevation of the study area and the distribution of AERONET sites.

The main inversion procedures in this paper include AHI data extraction, clipping to the study area, cloud and water mask, resampling, gas absorption correction, and a PSO solution.

Due to the requirement of two clear-sky observations, the accurate cloud mask will help improve the accuracy of the retrieval results. In this study, the process of the cloud mask algorithm is shown in Figure 3 [54–56].

The algorithm is suitable for AOD retrieval over various surface types including the water body [32]. However, we focus on AOD inversion over land. Thus, the MCD12C1 product is applied to mask the water body in the study area. In this way, the iterative computation time is also reduced.

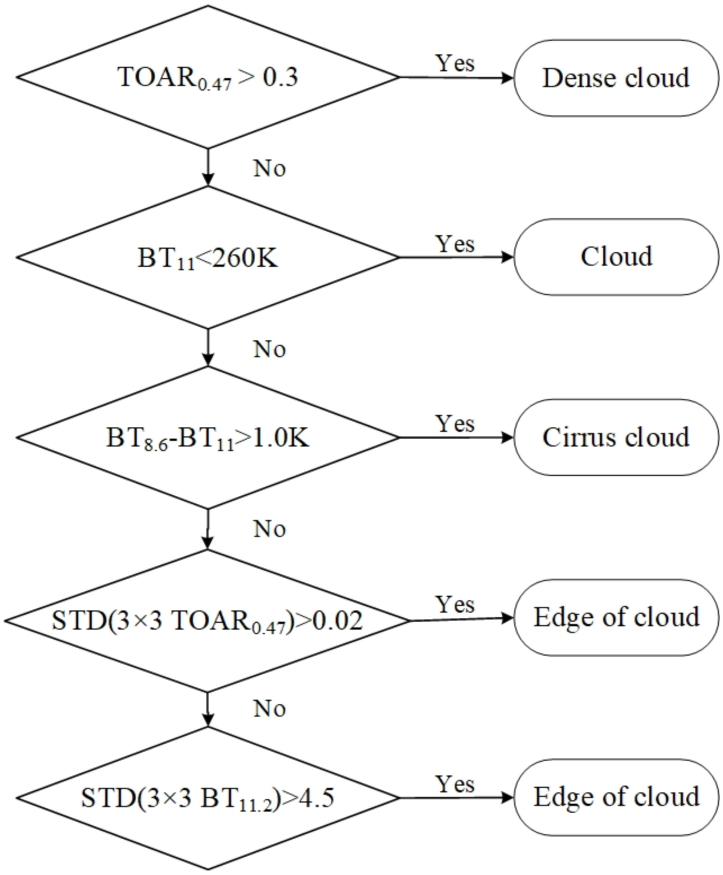

Figure 3. The flow chart of AHI cloud mask. TOAR: Top of atmosphere reflectance; BT: Brightness temperature; STD: Standard deviation.

Before the joint solution, we revised the TOAR observations for gas absorption according to the following formulas. Through multiplying TOAR by the reciprocal of total atmospheric transmittance T^{λ}_{Gas}, we obtained gas-corrected TOAR $TOAR^{\lambda}_{Cor}$. The atmospheric gases taken into consideration mainly include H_2O and O_3. T^{λ}_{other} is the transmittance of other gases. For the convenience of calculation, the optical thickness of each gas uses the fixed values in Table 1.

Table 1. The optical depth of gases used in gas absorption correction.

Wavelength (μm)	$\tau^{\lambda}_{H_2O}$	$\tau^{\lambda}_{O_3}$	τ^{λ}_{other}
0.47	8.0×10^{-5}	2.9×10^{-3}	1.25×10^{-3}
2.3	2.53×10^{-2}	2.0×10^{-5}	1.63×10^{-2}

$$TOAR^{\lambda}_{Cor} = TOAR^{\lambda} / T^{\lambda}_{Gas} \tag{5}$$

$$T^{\lambda}_{Gas} = T^{\lambda}_{H_2O} \cdot T^{\lambda}_{O_3} \cdot T^{\lambda}_{other} \tag{6}$$

The gas transmittance of each part is calculated as follows:

$$T^{\lambda}_{H_2O} = \exp\left(G \cdot \tau^{\lambda}_{H_2O}\right),\ T^{\lambda}_{O_3} = \exp\left(G \cdot \tau^{\lambda}_{O_3}\right),\ T^{\lambda}_{other} = \exp\left(G \cdot \tau^{\lambda}_{other}\right) \tag{7}$$

$$G = \frac{1}{\cos(\theta_S)} + \frac{1}{\cos(\theta_V)} \tag{8}$$

where G is air mass factor. θ_S and θ_V represent the zenith angle of the sun and sensor.

For every hour of cloud-free observation over the land, the following cost function is constructed for each matching pixel pair:

$$J(x) = \left(\frac{A^1_{0.47\mu m}}{A^2_{0.47\mu m}} - \frac{A^1_{2.3\mu m}}{A^2_{2.3\mu m}} \right)^2 \quad (9)$$

The PSO algorithm is used to minimize the cost function. Here, three terminal conditions are used to end PSO: (1) The cost function is less than the specified threshold, 1.0×10^{-7}; (2) the change of the optimal particle (AOD in the paper) is less than 1.0×10^{-7}, which means the solution tends to be stable; and (3) the number of iterations reaches 200. If any of the above conditions are met, PSO stops the iteration and outputs the results. It should be pointed out that the MODIS aerosol products were used to calculate the monthly maximum AOD value ($MODIS_{AODmax}$) of the study area, and the missing part was given by interpolation. The range of inversion value was set as [0, 2 $\times$ $MODIS_{AODmax}$] (if the upper limit of the range exceeds 4, set it to 4).

4. Result and Analysis

We applied the IBAA algorithm to AHI data to estimate hourly AOD over the Chinese mainland region from April to June 2019. In this section, we focus on evaluating IBAA AOD through comparisons with AERONET measurements, JAXA aerosol products, and MODIS C6.1 DB AOD. Furthermore, we analyzed the surface albedo result and IBAA performance in the coarse-particle aerosols case and evaluated the global optimization capability of PSO.

4.1. AOD Validation

In order to validate our algorithm, the ground-based measurements of 14 AERONET sites introduced in Section 2.3 were quantitatively compared with AHI-derived AOD of IBAA. In the meantime, we compared the JAXA AOD product of the same period with AERONET.

Because AERONET products do not provide AOD at 470 nm ($\tau_{470}^{AERONET}$), we utilize the following formula to calculate $\tau_{470}^{AERONET}$ based on the parameters "AOD_440 nm" and "440-675_Angstrom_Exponent" provided by AERONET [57]:

$$\tau_{470}^{AERONET} = \tau_{440}^{AERONET} \left(\frac{470}{440} \right)^{-\alpha} \quad (10)$$

where α refers to Angstrom exponent, and here it is the parameter "440-675_Angstrom_Exponent". $\tau_{440}^{AERONET}$ is AERONET AOD at 440 nm, and here it is the parameter "AOD_440 nm". We also calculated JAXA AOD at 470 nm (τ_{470}^{AHI}) by the Equation (9) due to only AOD at 500 nm (τ_{500}^{AHI}) provided.

$$\tau_{470}^{AHI} = \tau_{500}^{AHI} \left(\frac{470}{500} \right)^{-\alpha} \quad (11)$$

Due to the assumption that AOD does not vary in an hour, only AERONET AOD measurements matched within the two AHI observations' intervals are averaged for validation. The AHI-derived AODs were averaged at a 50 km $\times$ 50 km spatial window centered on AERONET sites. JAXA AODs were also averaged at a 50 km $\times$ 50 km spatial window, but with AERONET AOD, they averaged within $\pm$30 min of the satellite observation time [40]. Figure 4a shows the scatter plot of AHI IBAA AOD and AERONET AOD. The solid red and blue lines are the 1:1 line and EE $\pm$ (0.05 + 0.2 $\times$ $AOD_{AERONET}$) envelope lines. There are a total of 2079 matched points of AHI and AERONET AODs with good agreement in temporal variation and spatial distribution. The correlation coefficient R is 0.82, the RMSE is 0.27, and MD is 0.059. A total of 62.77% retrieval AODs fall within the uncertainty of ΔAOD = $\pm$(0.05 + 0.2 $\times$ $AOD_{AERONET}$). The IBAA algorithm shows a slight underestimation with 20.54% matched points below EE. AHI-derived AODs in almost all sites show great agreement with ground measurements. Only at the Pokhara and Lumbini_North sites are there obvious underestimates. The errors may be caused by the high satellite zenith angle (about 70 degrees), but the results still capture AOD variation over time as shown in Figure 5.

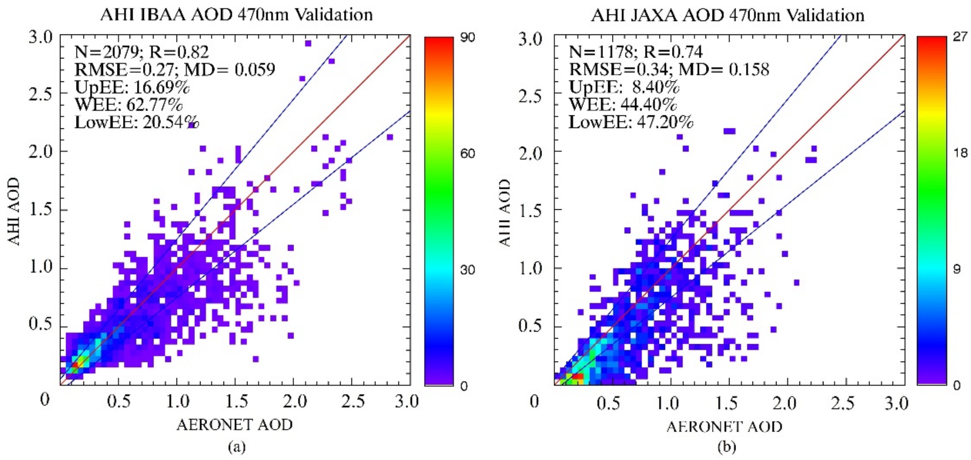

Figure 4. (**a**) The scatter plot of AHI IBAA AOD and AERONET AOD at 470 nm; (**b**) the scatter plot of AHI JAXA AOD and AERONET AOD at 470 nm. The color bars in (**a**) and (**b**) indicate the number of samples.

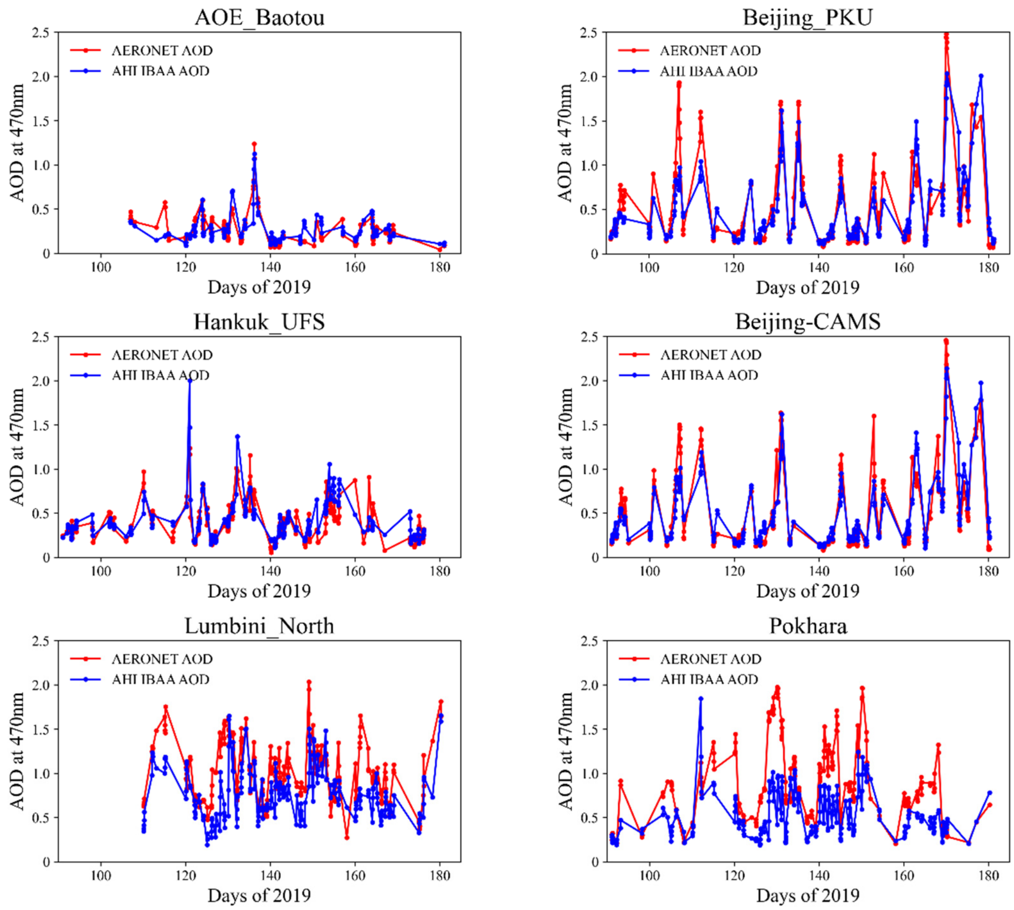

Figure 5. *Cont.*

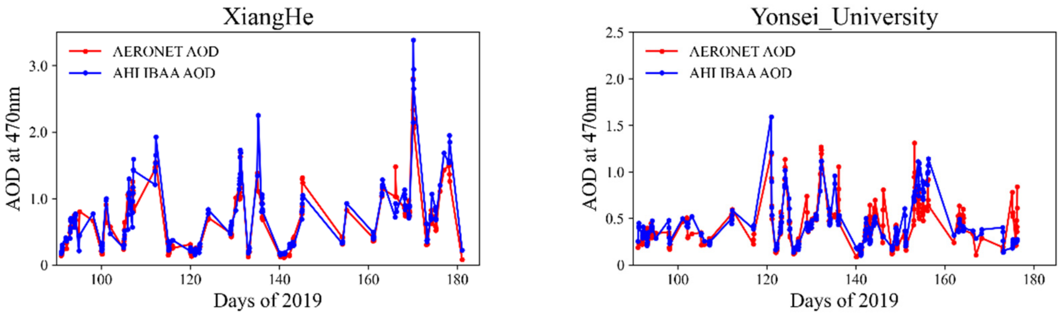

Figure 5. Variation curves of the hourly AOD (0.47 µm) from AHI IBAA and the AERONET product in eight AERONET stations during the study period. The red lines represent the matched AOD from AERONET and the blue lines are that from AHI.

The validation result of JAXA AOD is illustrated as Figure 4b. JAXA AOD has fewer matched points, with an R of 0.74 and RMSE of 0.34. It shows a large overestimation with 47.20% below EE, which is higher than the 44.40% falling within the EE line. Figure 6a,b shows the frequency of the distribution of AHI AOD and AERONET AOD differences, respectively. In general, the results of the IBAA algorithm are closer to the AERONET measurements. Additionally, we provide a detailed comparison of each site in Table 2, which illustrates our algorithm has high coverage and better accuracy over the Chinese mainland. In order to intuitively show the consistency between IBAA results and ground-based measurements on this time scale, we created the variation curves shown in Figure 5 for AERONET sites with matching points greater than 100. The time series of IBAA AHI AOD is consistent with the ground-based observation AOD at all 14 sites. However, the IBAA method slightly underestimates AOD, especially for high aerosol loading. This may be caused by aerosols with strong absorption, and IBAA does not take into account the specific aerosol type.

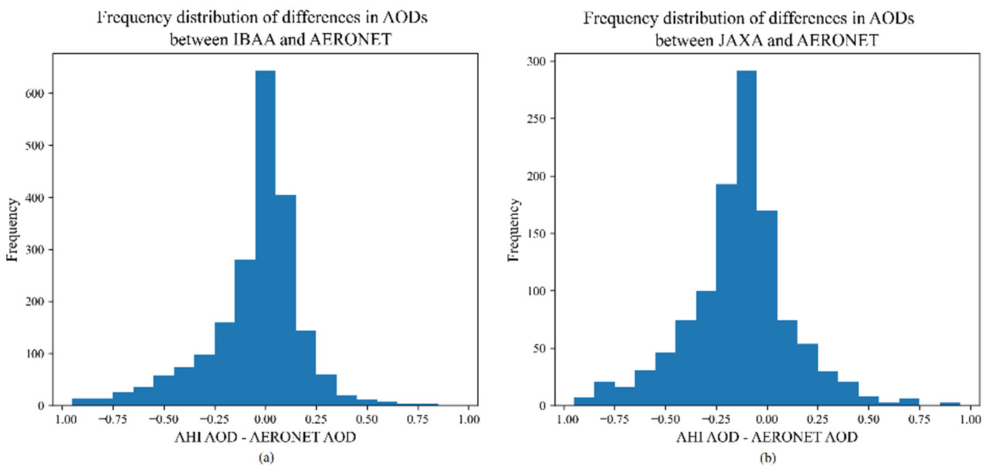

Figure 6. (**a**) The bar plot of frequency distribution of IBAA AOD - AERONET AOD; (**b**) the bar plot of frequency distribution of JAXA AOD - AERONET AOD.

Moreover, we compared IBAA AOD and MODIS DB AOD on 2 May 2019. Figure 7 shows the hourly variation of AHI AOD with good coverage and Figure 8 shows MODIS DB AOD of Terra and Aqua on the same day. From these two pictures, we can see that AHI-retrieved AOD has a similar spatial distribution to MODIS DB AOD. However, AHI seems to have lower AOD than MODIS in the dust area (especially Taklimakan Desert), which might be related to the assumption that the effect of aerosol is ignored at 2.3 µm. This will be analyzed in more detail in Section 4.3.

Table 2. The detailed AERONET stations information and comparisons between AERONET AOD with IBAA AOD and JAXA AOD.

Site Name	Latitude, Longitude	Altitude	Land Use and Cover	N-IBAA	R-IBAA	RMSE-IBAA	MD-IBAA	WEE-IBAA (%)	UpEE-IBAA (%)	LowEE-IBAA (%)	N-JAXA	R-JAXA	RMSE-JAXA	MD-JAXA	WEE-JAXA (%)	UpEE-JAXA (%)	LowEE-JAXA (%)
AOE_Baotou	40.85° N, 109.63° E	1314	Grasslands	146	0.83	0.11	−0.01	70.6	18.5	10.9	100	0.80	0.13	0.08	52.0	3.0	45.0
Beijing_PKU	39.99° N, 116.31° E	53	Urban and Build-Up Land	285	0.91	0.21	0.01	66.0	21.5	12.5	174	0.85	0.23	0.09	49.4	9.8	40.8
Beijing-CAMS	39.93° N, 116.32° E	106	Urban and Build-Up Land	288	0.88	0.25	0.06	60.3	17.9	21.8	176	0.88	0.21	0.06	51.7	9.1	39.2
Bhola	22.23° N, 90.76° E	7	Croplands	27	0.39	0.18	−0.12	77.8	22.2	0	40	0.66	0.42	0.34	32.5	0	67.5
Hankuk_UFS	37.34° N, 127.27° E	167	Deciduous Broadleaf Forest	249	0.80	0.15	−0.02	69.9	20.9	9.2	54	0.88	0.15	0.08	57.4	7.4	35.2
Hong_Kong_Sheung	22.48° N, 114.12° E	40	Savannas	17	0.85	0.21	−0.14	41.2	58.8	0	0	-	-	-	-	-	-
Lulin	23.47° N, 120.87° E	2868	Evergreen Broadleaf Forest	48	0.81	0.16	−0.14	31.3	68.7	0	30	0.82	0.08	0.05	80.0	0	20.0
Lumbini_North	27.50° N, 83.28° E	89	Croplands	225	0.55	0.38	0.23	55.1	4.0	40.9	181	0.31	0.59	0.33	30.4	10.5	59.1
Pokhara	28.19° N, 83.98° E	800	Savannas	230	0.63	0.48	0.33	33.9	3.9	62.2	152	0.82	0.42	0.32	29.6	0.7	69.7
Thimphu	27.47° N, 89.64° E	2314	Evergreen Needle-leaf Forest	6	0.94	0.04	0.02	100.0	0	0	0	-	-	-	-	-	-
Xianghe	39.75° N, 116.96° E	36	Croplands	213	0.92	0.23	−0.06	77.9	16.4	5.7	158	0.81	0.25	0.02	46.8	21.5	31.7
Xuzhou-CUMT	34.22° N, 117.14° E	59.7	Urban and Build-Up Land	48	0.80	0.19	−0.02	79.2	12.5	8.3	46	0.89	0.35	0.33	8.7	0	91.3
Yanqihu	40.41° N, 116.67° E	100	Grasslands	41	0.98	0.29	0.17	68.3	2.4	29.3	13	0.86	0.37	0.19	76.9	0	23.1
Yonsei_University	37.56° N, 126.94° E	97	Urban and Build-Up Land	256	0.76	0.17	−0.01	71.5	18.0	10.5	54	0.63	0.22	0.07	70.4	9.3	20.3

The land use and cover types are from MCD12C1 product. N is the total matched points of each AERONET station. R is the correlation coefficient and RMSE is the root-mean-square error, MD is the mean difference and represents the average value of all AERONET-matched AOD minus AHI AOD. EE is the expected error of $\pm(0.05 + 0.2 \times AOD_{AERONET})$ according to other studies [24,25]. WEE is the percentage of points falling within the EE envelope and UpEE and LowEE are above and below EE envelope. '-' means no valid value here.

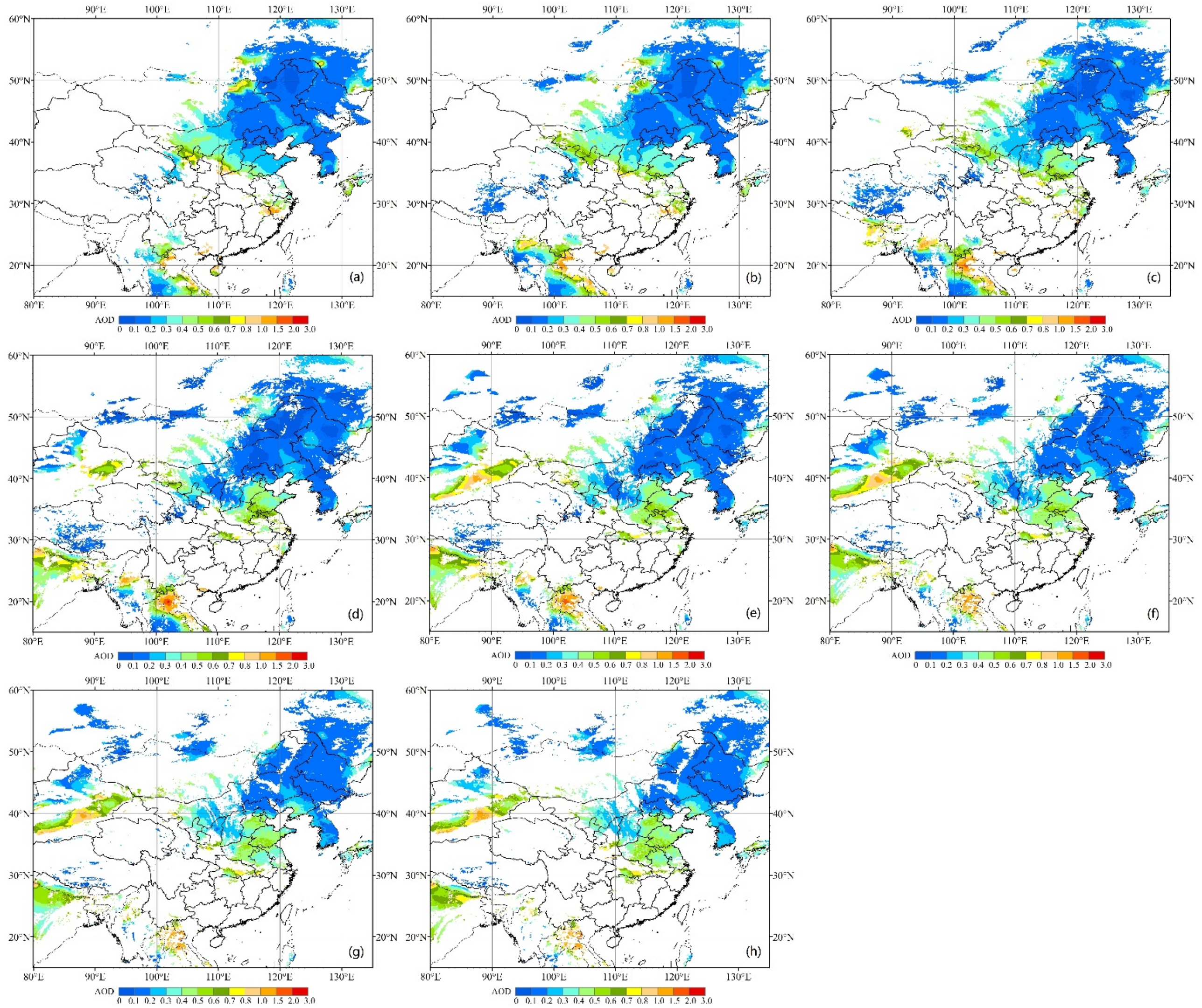

Figure 7. AHI-retrieved AOD on 2 May 2019. (**a**–**h**) Hourly AOD retrieved from 00:00 UTC to 08:00 UTC (Universal Time Coordinated), respectively.

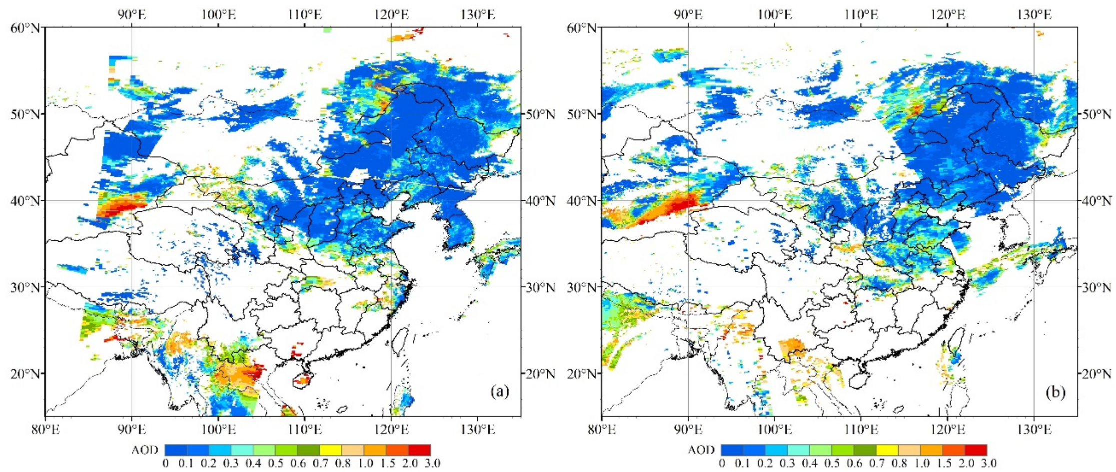

Figure 8. MODIS DB AOD on 2 May 2019 (**a**) for Terra-MODIS and (**b**) for Aqua-MODIS.

4.2. Surface Albedo Result

The IBAA algorithm also obtained the surface albedo at 0.47 µm. Here, we conducted a preliminary analysis of the results. For those observations that were used for inversion by both the previous and the later time, we combined the albedo results obtained from the two times to obtain better spatial coverage (taking the average when both have valid values). As Figure 9 shows, the surface albedo at 0.47 µm changes significantly, and this variation seems to be independent of the change in the solar elevation angle [58]. To determine this factor, we analyzed the surface albedo at 2.3 µm (as illustrated in Figure 10) and found that the surface albedo of AHI at 0.47 and 2.3 µm has the same change trend over time. According to Equation (2), the ratio of surface albedo at 0.47 µm at adjacent times is equal to the ratio of the surface albedo at 2.3 µm. Therefore, the surface albedo at 0.47 µm has the same daily variation trend as that at 2.3 µm.

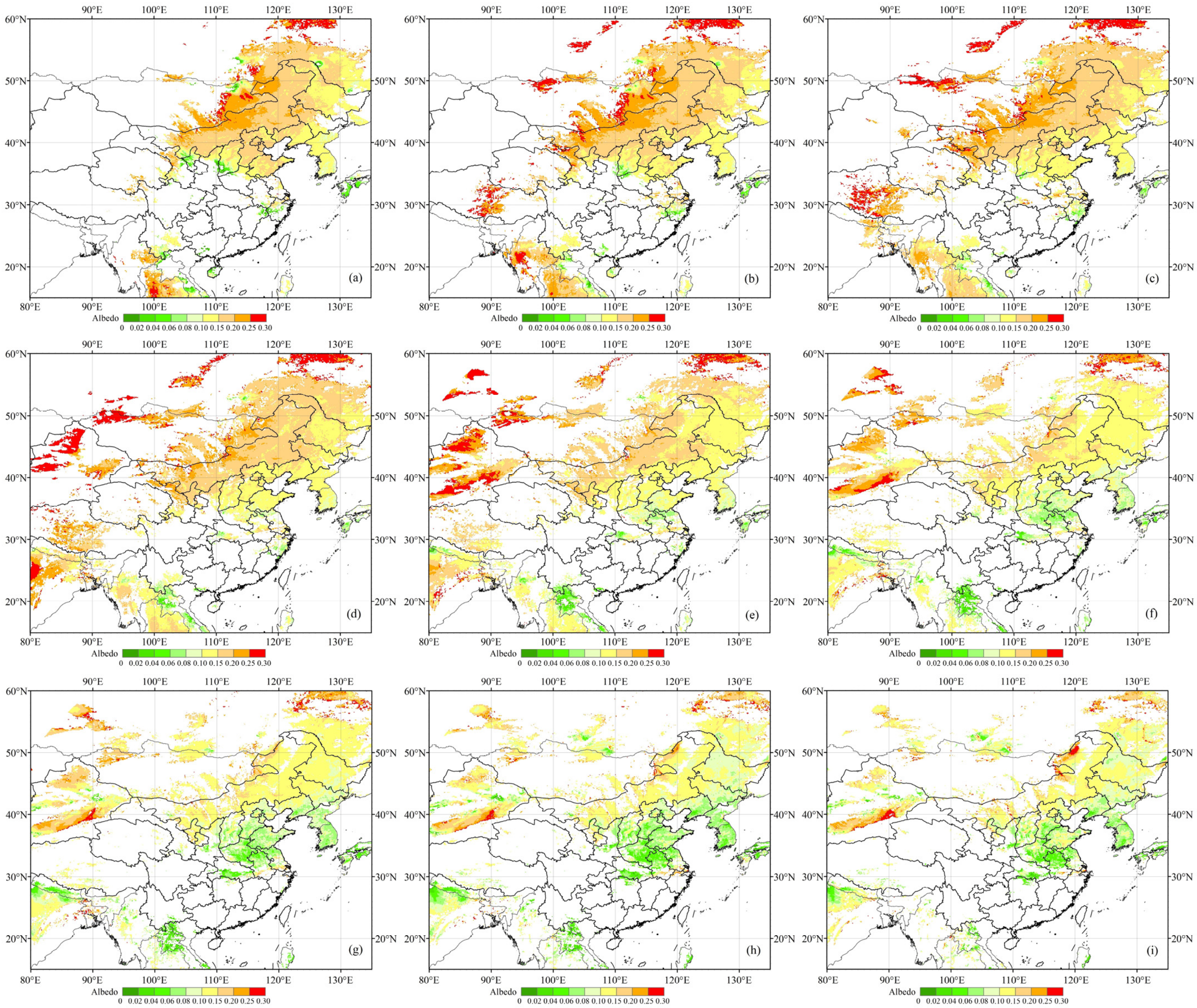

Figure 9. AHI-retrieved surface albedo at 0.47 µm on 2 May 2019. (**a**–**i**) Hourly albedo from 00:00 UTC to 08:00 UTC, respectively.

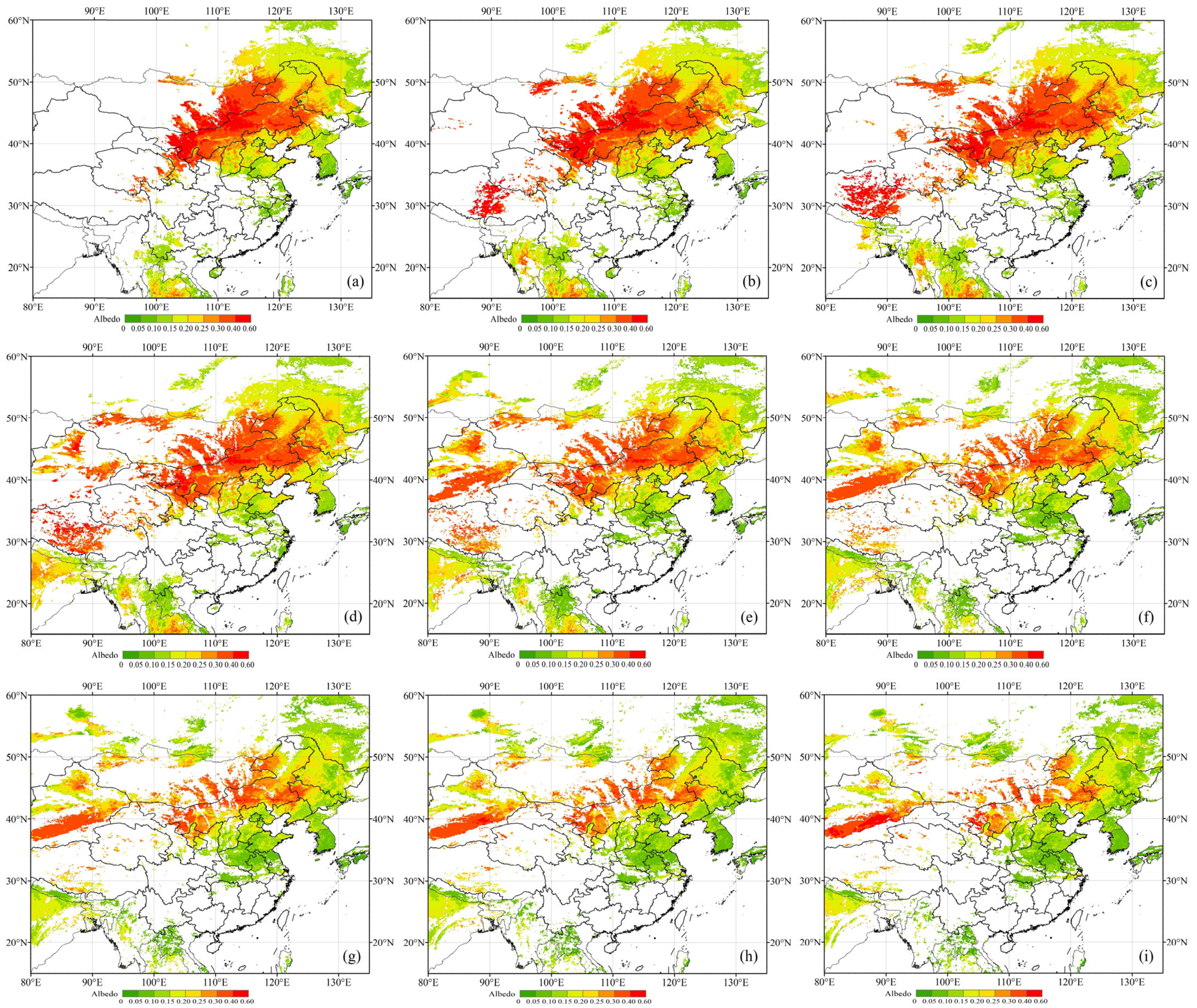

Figure 10. AHI surface albedo at 2.3 µm on 2 May 2019. (**a**–**i**) Hourly albedo from 00:00 UTC to 08:00 UTC, respectively.

4.3. PSO and Coarse Aerosols Analysis

First, in order to test the PSO capability of global optimization and the suitability of the AOD inversion range setting, we selected the observations over the Beijing-CAMS site on 3 April 2019 for analysis. AHI observations are available for AOD inversion from 00:00 UTC to 08:00 UTC on this day. Through changing the value of the upper boundary of the AOD range, we found that as the upper boundary increases, IBAA AODs are close to the final retrieval results and remain unchanged when the upper boundary is greater than 1 as illustrated in Figure 11. Here, the upper limit calculated according to MODIS AOD is 1.77 and it completely satisfies the condition of obtaining a global optimal solution by PSO. Because the initialization of particles is random and the AOD result is stable, there is no need to worry that the algorithm will enter a local optimal solution. In addition, the boundaries of the AOD range in the paper are reasonable and almost all IBAA AODs are within the set range.

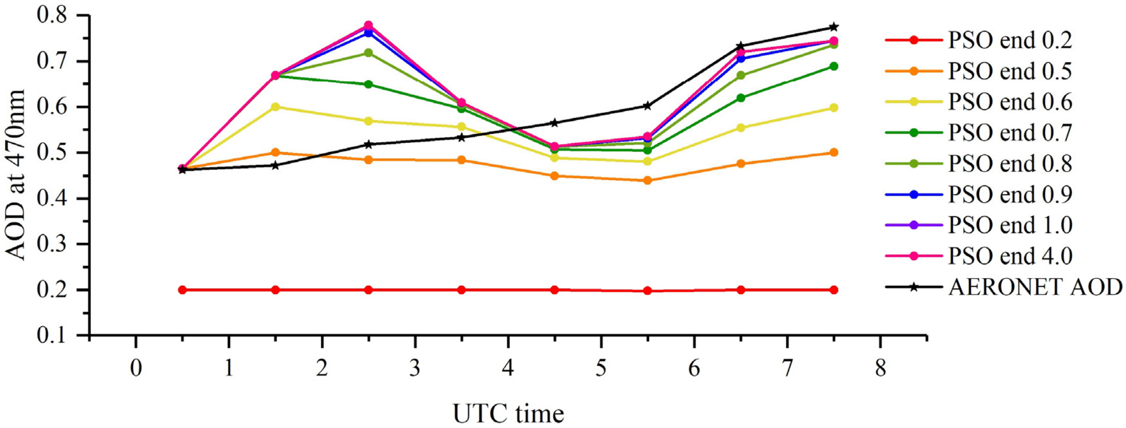

Figure 11. IBAA AOD with different upper boundary settings in PSO in Beijing-CAMS on 3 April 2019. PSO end refers to the upper limit of AOD range in PSO. The black line with the star mark is Beijing-CAMS observation AOD.

Second, we evaluated the performance of the IBAA algorithm in the large-particle aerosols situation. The assumption regarding neglecting the aerosol effect at 2.3 μm is unreasonable in the coarse-aerosol model. The Angstrom exponent α can indicate the aerosol particle size (the smaller the α value, the larger the particle diameter), so we analyzed the distribution of α and the IBAA AOD relative error. As Figure 12 shows, we find that IBAA AOD has lower relative error when α is large. However, the big difference from our prediction is that when α is less than 0.3, the relative error is small. We examined this and found that most of the AOD is also small (less than 0.3). This may result from sampling uncertainties due to having very few samples for such small alpha values. In addition, we analyzed IBAA AOD when AERONET AOD is greater than 0.5 and α is less than 1. We were able to find fairly large errors with RMSE = 0.33 and a low correlation between IBAA AOD and AERONET AOD from Figure 13 in this case.

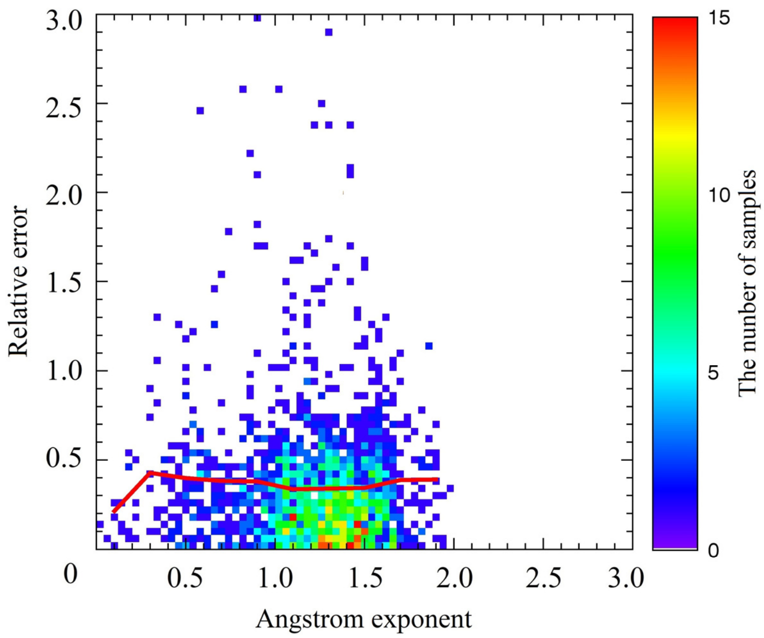

Figure 12. The scatter plot of Angstrom exponent and IBAA AOD relative error (relative error = $|AOD_{IBAA} - AOD_{AERONET}| / AOD_{AERONET}$). The red line represents the IBAA AOD average relative error.

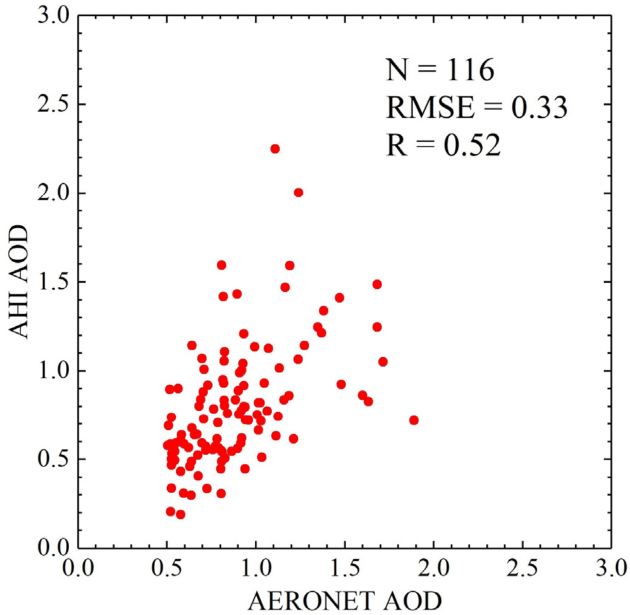

Figure 13. The scatter plot of IBAA AOD and AERONET AOD at 470 nm with AERONET AOD > 0.5 and Angstrom exponent < 1.

5. Conclusions

In this paper, we proposed an algorithm IBAA to jointly retrieve Himawari-8 AHI AOD and the surface albedo. The algorithm is applied to the Chinese mainland from April to June 2019. Using the theory of Xue and Cracknell's two-angle inversion of the surface albedo [30], we retrieved AOD and the surface albedo at 0.47 μm using the particle swarm optimization method with the assumption that AOD does not vary between two observations within a one-hour interval. The IBAA algorithm is applicable for different land cover types and does not consider aerosol types.

The AHI-derived AODs from the entire study period were evaluated against 14 ground-based AERONET measurements and qualitatively compared with JAXA AODs. AHI IBAA AOD shows good agreement with AERONET measurements with 62.77% retrieval falling within the uncertainty of $\Delta AOD = \pm(0.05 + 0.2 \times AOD_{AERONET})$ and a high correlation coefficient of 0.82, which is better than JAXA AOD (44.4% and 0.74). We also compared IBAA AOD with the MODIS C6.1 DB AOD product, and they generally show similar spatial distributions. Moreover, the PSO solution displays an excellent ability to achieve global optimization of AHI AOD. Though IBAA does not perform well in the case of coarse-particle aerosols, IBAA AOD has better accuracy and coverage than JAXA V030 AOD overall.

With the comparison between Himawari-8 IBAA and other AHI algorithms in previous papers, such as different improved DT algorithms (R = 0.86 and RMSE = 0.12 in [21], 2018; R = 0.9 and RMSE = 0.15 in [22]; R > 0.8 in [23]), an improved time-series algorithm (R > 0.8 and RMSE < 0.2 in [59]), the OE method (R = 0.88, RMSE = 0.17 and 69.9% of retrievals falling within $EE = \pm(0.05 + 0.2 \times AOD_{AERONET})$ in [24]), and the monthly spectral base reflectance ratio library method (R = 0.939, RMSE = 0.113 and 82.5% of retrievals falling within $EE = \pm(0.05 + 0.2 \times AOD_{AERONET}$ in [25]), the IBAA algorithm has certain precision and a simple process. Due to different time range and regions and different ground-based station observation selected for algorithm validation applied in the above papers, there are great uncertainties in such comparisons. The PSO method in the paper performs well in global optimization, which may be a better method of numerical solutions in quantitative inversion in remote sensing.

In the future, there will be additional work to be conducted to address several issues. First, more spectral band information needs to be taken into consideration to retrieve AOD.

Second, certain parameters in the IBAA algorithm, such as the backscattering coefficient and the optical depth of atmospheric gases, need to be determined more accurately, which may be obtained from other products containing these parameters or through improving the algorithm. Third, more results should be calculated to better evaluate the IBAA AOD from a longer period. Moreover, more attention should be paid to analyzing the surface albedo in detail.

Author Contributions: Conceptualization, Y.X.; methodology, C.J.; software, C.J.; validation, X.J. and C.J.; formal analysis, X.J.; investigation, S.W. and X.J.; resources, Y.X.; data curation, Y.S.; writing—original draft preparation, CL.J.; writing—review and editing, Y.X. and CL.J.; visualization, C.J.; supervision, Y.X.; project administration, Y.X.; funding acquisition, Y.X. All authors have read and agreed to the published version of the manuscript.

Funding: This work was supported in part by the National Natural Science Foundation of China (NSFC) under Grant No. 41871260.

Institutional Review Board Statement: Not applicable.

Informed Consent Statement: Not applicable.

Data Availability Statement: Not applicable.

Acknowledgments: The authors thank all data providers for their effort in making the data available: MODIS data from NASA MODIS LAADS, AHI data from P-Tree System, Japan Aerospace Exploration Agency, and AERONET products from NASA and PHO-TONS.

Conflicts of Interest: The authors declare no conflict of interest.

References

1. Hansen, J.; Sato, M.; Ruedy, R. Radiative forcing and climate response. *J. Geophys. Res. Atmos.* **1997**, *102*, 6831–6864. [CrossRef]
2. Anderson, T.L.; Charison, R.J.; Schwartz, S.E.; Knutti, R.; Boucher, O.; Rodhe, H. Climate forcing by aerosols—A hazy picture. *Science* **2003**, *300*, 1103–1104. [CrossRef] [PubMed]
3. Colbeck, I.; Lazaridis, M. Aerosols and environmental pollution. *Naturwissenschaften* **2009**, *97*, 117–131. [CrossRef] [PubMed]
4. Hu, X.Q.; Lu, N.M.; Niu, T.; Zhang, P. Operational retrieval of Asian sand and dust storm from FY-2C geostationary meteorological satellite and its application to real time forecast in Asia. *Atmos. Chem. Phys. Discuss.* **2008**, *8*, 1649–1659. [CrossRef]
5. Sowden, M.; Mueller, U.; Blake, D. Review of surface particulate monitoring of dust events using geostationary satellite remote sensing. *Atmos. Environ.* **2018**, *183*, 154–164. [CrossRef]
6. Shin, Y.-R.; Sohn, E.-H.; Park, K.-H.; Ryu, G.-H.; Lee, S.; Lee, S.-Y.; Park, N.-Y. Improved dust detection over east asia using geostationary satellite data. *Asia-Pac. J. Atmos. Sci.* **2021**, *57*, 787–798. [CrossRef]
7. Wei, X.; Chang, N.-B.; Bai, K.; Gao, W. Satellite remote sensing of aerosol optical depth: advances, challenges, and perspectives. *Crit. Rev. Environ. Sci. Technol.* **2020**, *50*, 1640–1725. [CrossRef]
8. Knapp, K.; Frouin, R.; Kondragunta, S.; Prados, A. Toward aerosol optical depth retrievals over land from GOES visible radiances: determining surface reflectance. *Int. J. Remote Sens.* **2005**, *26*, 4097–4116. [CrossRef]
9. Popp, C.; Hauser, A.; Foppa, N.; Wunderle, S. Remote sensing of aerosol optical depth over central Europe from MSG-SEVIRI data and accuracy assessment with ground-based AERONET measurements. *J. Geophys. Res. Space Phys.* **2007**, *112*, D24S11.1-16. [CrossRef]
10. Lee, J.; Kim, J.; Song, C.H.; Ryu, J.-H.; Ahn, Y.-H. Algorithm for retrieval of aerosol optical properties over the ocean from the Geostationary Ocean Color Imager. *Remote Sens. Environ.* **2010**, *114*, 1077–1088. [CrossRef]
11. Choi, M.; Kim, J.; Lee, J.; Kim, M.; Park, Y.-J.; Jeong, U.; Kim, W.; Hong, H.; Holben, B.; Eck, T.F.; et al. GOCI Yonsei Aerosol Retrieval (YAER) algorithm and validation during the DRAGON-NE Asia 2012 campaign. *Atmos. Meas. Tech.* **2016**, *9*, 1377–1398. [CrossRef]
12. Kim, J.; Yoon, J.; Ahn, M.H.; Sohn, B.J.; Lim, H.S. Retrieving aerosol optical depth using visible and mid-IR channels from geostationary satellite MTSAT-1R. *Int. J. Remote Sens.* **2008**, *29*, 6181–6192. [CrossRef]
13. Kim, M.; Kim, J.; Wong, M.S.; Yoon, J.; Lee, J.; Wu, D.; Chan, P.W.; Nichol, J.E.; Chung, C.-Y.; Ou, M.-L. Improvement of aerosol optical depth retrieval over Hong Kong from a geostationary meteorological satellite using critical reflectance with background optical depth correction. *Remote Sens. Environ.* **2014**, *142*, 176–187. [CrossRef]
14. Thomas, G.E.; Carboni, E.; Sayer, A.M.; Poulsen, C.A.; Grainger, R.G. Oxford-RAL Aerosol and Cloud (ORAC): Aerosol retrievals from satellite radiometers. In *Satellite Aerosol Remote Sensing over Land*; Kokhanovsky, A.A., de Leeuw, G., Eds.; Springer Praxis Books: Berlin/Heidelberg, Germany, 2009. [CrossRef]

15. Zhang, H.; Lyapustin, A.; Wang, Y.; Kondragunta, S.; Laszlo, I.; Ciren, P.; Hoff, R.M. A multi-angle aerosol optical depth retrieval algorithm for geostationary satellite data over the United States. *Atmos. Chem. Phys. Discuss.* **2011**, *11*, 11977–11991. [CrossRef]
16. Mei, L.; Xue, Y.; De Leeuw, G.; Holzer-Popp, T.; Guang, J.; Li, Y.; Yang, L.; Xu, H.; Xu, X.; Li, C.; et al. Retrieval of aerosol optical depth over land based on a time series technique using MSG/SEVIRI data. *Atmos. Chem. Phys.* **2012**, *12*, 9167–9185. [CrossRef]
17. Govaerts, Y.; Wagner, S.; Lattanzio, A.; Watts, P. Application of the Optimal Estimation Method to the Joint Retrieval of Aerosol Load and Surface Reflectance from MSG/SEVIRI. *Observations* **2009**, *1100*, 255–258. [CrossRef]
18. Zhang, T.; Zang, L.; Mao, F.; Wan, Y.; Zhu, Y. Evaluation of Himawari-8/AHI, MERRA-2, and CAMS Aerosol Products over China. *Remote Sens.* **2020**, *12*, 1684. [CrossRef]
19. ABI AOD ATBD. GOES-R Advanced Baseline Imager (ABI) Algorithm Theoretical Basis Document for Suspended Matter/Aerosol Optical Depth and Aerosol Size Parameter. NOAA/NESDIS/STAR, Version 4.2. 14 February 2018. Available online: https://www.star.nesdis.noaa.gov/goesr/documents/ATBDs/Baseline/ATBD_GOES-R_Aerosol_Optical_Depth_v4.2_Feb2018.pdf (accessed on 14 November 2021).
20. Xie, Y.; Xue, Y.; Guang, J.; Mei, L.; She, L.; Li, Y.; Che, Y.; Fan, C. Deriving a Global and Hourly Data Set of Aerosol Optical Depth Over Land Using Data From Four Geostationary Satellites: GOES-16, MSG-1, MSG-4, and Himawari-8. *IEEE Trans. Geosci. Remote Sens.* **2019**, *58*, 1538–1549. [CrossRef]
21. Zhang, W.; Xu, H.; Zheng, F. Aerosol optical depth retrieval over east Asia using Himawari-8/AHI data. *Remote Sens.* **2018**, *10*, 137. [CrossRef]
22. Ge, B.; Li, Z.; Liu, L.; Yang, L.; Chen, X.; Hou, W.; Zhang, Y.; Li, D.; Li, L.; Qie, L. A Dark Target method for Himawari-8/AHI aerosol retrieval: Application and validation. *IEEE Trans. Geosci. Remote. Sens.* **2018**, *57*, 381–394. [CrossRef]
23. Gao, L.; Chen, L.; Li, J.; Zhu, L. An improved dark target method for aerosol optical depth retrieval over China from Himawari-8. *Atmos. Res.* **2021**, 250. [CrossRef]
24. She, L.; Xue, Y.; Yang, X.; Leys, J.; Guang, J.; Che, Y.; Fan, C.; Xie, Y.; Li, Y. Joint Retrieval of Aerosol Optical Depth and Surface Reflectance Over Land Using Geostationary Satellite Data. *IEEE Trans. Geosci. Remote Sens.* **2018**, *57*, 1489–1501. [CrossRef]
25. Su, X.; Wang, L.; Zhang, M.; Qin, W.; Bilal, M. A High-Precision Aerosol Retrieval Algorithm (HiPARA) for Advanced Himawari Imager (AHI) data: Development and verification. *Remote Sens. Environ.* **2020**, *253*, 112221. [CrossRef]
26. Yan, X.; Li, Z.; Luo, N.; Shi, W.; Zhao, W.; Yang, X.; Jin, J. A minimum albedo aerosol retrieval method for the new-generation geostationary meteorological satellite Himawari-8. *Atmos. Res.* **2018**, *207*, 14–27. [CrossRef]
27. Shi, S.; Cheng, T.; Gu, X.; Letu, H.; Guo, H.; Chen, H.; Wang, Y.; Wu, Y. Synergistic Retrieval of Multitemporal Aerosol Optical Depth Over North China Plain Using Geostationary Satellite Data of Himawari-8. *J. Geophys. Res. Atmos.* **2018**, *123*, 5525–5537. [CrossRef]
28. Zhang, H.; Kondragunta, S.; Laszlo, I.; Zhou, M. Improving GOES Advanced Baseline Imager (ABI) aerosol optical depth (AOD) retrievals using an empirical bias correction algorithm. *Atmos. Meas. Tech.* **2020**, *13*, 5955–5975. [CrossRef]
29. Zang, Z.; Li, D.; Guo, Y.; Shi, W.; Yan, X. Superior $PM_{2.5}$ Estimation by Integrating Aerosol Fine Mode Data from the Himawari-8 Satellite in Deep and Classical Machine Learning Models. *Remote Sens.* **2021**, *13*, 2779. [CrossRef]
30. Xue, Y.; Cracknell, A.P. Operational bi-angle approach to retrieve the Earth surface albedo from AVHRR data in the visible band. *Int. J. Remote Sens.* **1995**, *16*, 417–429. [CrossRef]
31. Li, Y.; Xue, Y.; He, X.; Guang, J. High-resolution aerosol remote sensing retrieval over urban areas by synergetic use of HJ-1 CCD and MODIS data. *Atmos. Environ.* **2011**. [CrossRef]
32. Xue, Y.; He, X.; Xu, H.; Guang, J.; Guo, J.; Mei, L. China Collection 2.0: The aerosol optical depth dataset from the synergetic retrieval of aerosol properties algorithm. *Atmos. Environ.* **2014**, *95*, 45–58. [CrossRef]
33. Kikuchi, M.; Murakami, H.; Suzuki, K.; Nagao, T.M.; Higurashi, A. Improved Hourly Estimates of Aerosol Optical Thickness Using Spatiotemporal Variability Derived From Himawari-8 Geostationary Satellite. *IEEE Trans. Geosci. Remote Sens.* **2018**, *56*, 3442–3455. [CrossRef]
34. Yoshida, M.; Kikuchi, M.; Nagao, T.M.; Murakami, H.; Nomaki, T.; Higurashi, A. Common Retrieval of Aerosol Properties for Imaging Satellite Sensors. *J. Meteorol. Soc. Jpn.* **2018**, 193–209. [CrossRef]
35. Levy, R.C.; Mattoo, S.; Munchak, L.A.; Remer, L.A.; Sayer, A.M.; Patadia, F.; Hsu, N.C. The Collection 6 MODIS aerosol products over land and ocean. *Atmos. Meas. Tech.* **2013**, *6*, 2989–3034. [CrossRef]
36. Che, H.; Yang, L.; Liu, C.; Xia, X.; Wang, Y.; Wang, H.; Wang, H.; Lu, X.; Zhang, X. Long-term validation of MODIS C6 and C6.1 Dark Target aerosol products over China using CARSNET and AERONET. *Chemosphere* **2019**, *236*, 124268. [CrossRef]
37. Wang, Y.; Yuan, Q.; Li, T.; Shen, H.; Zheng, L.; Zhang, L. Evaluation and comparison of MODIS Collection 6.1 aerosol optical depth against AERONET over regions in China with multifarious underlying surfaces. *Atmos. Environ.* **2018**, *200*, 280–301. [CrossRef]
38. Huang, G.; Chen, Y.; Li, Z.; Liu, Q.; Wang, Y.; He, Q.; Liu, T.; Liu, X.; Zhang, Y.; Gao, J.; et al. Validation and accuracy analysis of the Collection 6.1 MODIS aerosol optical depth over the westernmost city in china based on the sun-sky radiometer observations from SONET. *Earth Space Sci.* **2020**, *7*, e2019EA001041. [CrossRef]
39. Giles, D.M.; Sinyuk, A.; Sorokin, M.G.; Schafer, J.S.; Smirnov, A.; Slutsker, I.; Eck, T.F.; Holben, B.N.; Lewis, J.R.; Campbell, J.R.; et al. Advancements in the Aerosol Robotic Network (AERONET) Version 3 database–automated near-real-time quality control algorithm with improved cloud screening for Sun photometer aerosol optical depth (AOD) measurements. *Atmos. Meas. Tech.* **2019**, *12*, 169–209. [CrossRef]

40. Ichoku, C.; Chu, D.A.; Mattoo, S.; Kaufman, Y.J.; Remer, L.A.; Tanré, D.; Slutsker, I.; Holben, B.N. A spatio-temporal approach for global validation and analysis of MODIS aerosol products. *Geophys. Res. Lett.* **2002**, *29*. [CrossRef]
41. Flowerdew, R.J.; Haigh, J.D. Retrieval of aerosol optical thickness over land using the ATSR-2 Dual-Look Satellite Radiometer. *Geophys. Res. Lett.* **1996**, *23*, 351–354. [CrossRef]
42. Veefkind, J.P.; De Leeuw, G.; Stammes, P.; Koelemeijer, R.B. Regional distribution of aerosol over land, derived from ATSR-2 and GOME. *Remote Sens. Environ.* **2000**, *74*, 377–386. [CrossRef]
43. Yamamoto, Y.; Ichii, K.; Higuchi, A.; Takenaka, H. Geolocation accuracy assessment of Himawari-8/AHI imagery for application to terrestrial monitoring. *Remote Sens.* **2020**, *12*, 1372. [CrossRef]
44. Govaerts, Y.M.; Wagner, S.; Lattanzio, A.; Watts, P. Joint retrieval of surface reflectance and aerosol optical depth from MSG/SEVIRI observations with an optimal estimation approach: 1 Theory. *J. Geophys. Res.* **2010**, *115*, D02203.1-16. [CrossRef]
45. Dubovik, O.; Herman, M.; Holdak, A.; Lapyonok, T.; Tanré, D.; Deuzé, J.L.; Ducos, F.; Sinyuk, A.; Lopatin, A. Statistically optimized inversion algorithm for enhanced retrieval of aerosol properties from spectral multi-angle polarimetric satellite observations. *Atmos. Meas. Tech.* **2011**, *4*, 975–1018. [CrossRef]
46. Saleh, K.; Wigneron, J.P.; Waldteufel, P.; De Rosnay, P.; Schwank, M.; Calvet, J.C.; Kerr, Y.H. Estimates of surface soil moisture under grass covers using L-band radiometry. *Remote Sens. Environ.* **2007**, *109*, 42–53. [CrossRef]
47. Baret, F.; Buis, S. Estimating canopy characteristics from remote sensing observations: Review of methods and associated problems. *Adv. Land Remote Sens.* **2008**, 173–201.
48. Wigneron, J.P.; Jackson, T.J.; O'neill, P.; De Lannoy, G.; De Rosnay, P.; Walker, J.P.; Ferrazzoli, P.; Mironov, V.; Bircher, S.; Grant, J.P.; et al. Modelling the passive microwave signature from land surfaces: A review of recent results and application to the L-band SMOS & SMAP soil moisture retrieval algorithms. *Remote Sens. Environ.* **2017**, *192*, 238–262.
49. Kennedy, J.; Eberhart, R. Particle swarm optimization. In Proceedings of the ICNN'95-International Conference on Neural Networks, Perth, WA, Australia, 27 November–1 December 1995; pp. 1942–1948.
50. Wang, L.; Geng, H.; Liu, P.; Lu, K.; Kolodziej, J.; Ranjan, R.; Zomaya, A.Y. Particle Swarm Optimization based dictionary learning for remote sensing big data. *Knowl. Based Syst.* **2015**, *79*, 43–50. [CrossRef]
51. Venkateswaran, K.; Sowmya Shree, T.; Kousika, N.; Kasthuri, N. Performance analysis of ga and pso based feature selection techniques for improving classification accuracy in remote sensing images. *Indian J. Sci. Technol.* **2016**, *9*, 1–7. [CrossRef]
52. Shen, L.; Huang, X.; Fan, C. Double-Group Particle Swarm Optimization and Its Application in Remote Sensing Image Segmentation. *Sensors* **2018**, *18*, 1393. [CrossRef] [PubMed]
53. Gao, Y.; Li, Q.; Wang, S.; Gao, J. Adaptive neural network based on segmented particle swarm optimization for remote-sensing estimations of vegetation biomass. *Remote Sens. Environ.* **2018**, *211*, 248–260. [CrossRef]
54. Hsu, N.C.; Jeong, M.-J.; Bettenhausen, C.; Sayer, A.; Hansell, R.; Seftor, C.S.; Huang, J.; Tsay, S.-C. Enhanced Deep Blue aerosol retrieval algorithm: The second generation. *J. Geophys. Res. Atmos.* **2013**, *118*, 9296–9315. [CrossRef]
55. Wang, Y.; Chen, P.; Liu, C.; Zhang, Y. Size effect of circular concrete-filled steel tubular short columns subjected to axial compression. *Thin-Walled Struct.* **2017**, *120*, 397–407. [CrossRef]
56. Lim, H.; Choi, M.; Kim, J.; Kasai, Y.; Chan, P.W. AHI/Himawari-8 Yonsei Aerosol Retrieval (YAER): Algorithm, Validation and Merged Products. *Remote Sens.* **2018**, *10*, 699. [CrossRef]
57. Roman, M.O.; Gatebe, C.K.; Shuai, Y.; Wang, Z.; Gao, F.; Masek, J.G.; He, T.; Liang, S.; Schaaf, C.B. Use of In Situ and Airborne Multiangle Data to Assess MODIS- and Landsat-Based Estimates of Directional Reflectance and Albedo. *IEEE Trans. Geosci. Remote Sens.* **2013**, *51*, 1393–1404. [CrossRef]
58. Ångström, A. The parameters of atmospheric turbidity. *Tellus* **1964**, *16*, 64–75. [CrossRef]
59. Li, D.; Qin, K.; Wu, L.; Mei, L.; De Leeuw, G.; Xue, Y.; Shi, Y.; Li, Y. Himawari-8-Derived Aerosol Optical Depth Using an Improved Time Series Algorithm Over Eastern China. *Remote Sens.* **2020**, *12*, 978. [CrossRef]